PHOTONICS Research

Observation of a manifold in the chaotic phase space of an asymmetric optical microcavity

Yan-Jun Qian,[1,†] Qi-Tao Cao,[1,†] Shuai Wan,[2] Yu-Zhong Gu,[1] Li-Kun Chen,[1] Chun-Hua Dong,[2,6] Qinghai Song,[3,4,7] Qihuang Gong,[1,3,5] and Yun-Feng Xiao[1,3,5,8]

[1]State Key Laboratory for Mesoscopic Physics and Frontiers Science Center for Nano-optoelectronics, School of Physics, Peking University, Beijing 100871, China
[2]Key Laboratory of Quantum Information, University of Science and Technology of China, Hefei 230026, China
[3]Collaborative Innovation Center of Extreme Optics, Shanxi University, Taiyuan 030006, China
[4]Department of Electronic and Information Engineering, Shenzhen Graduate School, Harbin Institute of Technology, Shenzhen 518055, China
[5]Peking University Yangtze Delta Institute of Optoelectronics, Nantong 226010, China
[6]e-mail: chunhua@ustc.edu.cn
[7]e-mail: qinghai.song@hit.edu.cn
[8]e-mail: yfxiao@pku.edu.cn

Received 13 November 2020; revised 14 January 2021; accepted 14 January 2021; posted 15 January 2021 (Doc. ID 414785); published 1 March 2021

Chaotic dynamics in optical microcavities, governed dominantly by manifolds, is of great importance for both fundamental studies and photonic applications. Here, we report the experimental observation of a stable manifold characterized by energy and momentum evolution in the nearly chaotic phase space of an asymmetric optical microcavity. By controlling the radius of a fiber coupler and the coupling azimuth of the cavity, corresponding to the momentum and position of the input light, the injected light can in principle excite the system from a desired position in phase space. It is found that once the input light approaches the stable manifold, the angular momentum of the light experiences a rapid increase, and the energy is confined in the cavity for a long time. Consequently, the distribution of the stable manifold is visualized by the output power and the coupling depth to high-Q modes extracted from the transmission spectra, which is consistent with theoretical predictions by the ray model. This work opens a new path to understand the chaotic dynamics and reconstruct the complex structure in phase space, providing a new paradigm of manipulating photons in wave chaos.

https://doi.org/10.1364/PRJ.414785

1. INTRODUCTION

Chaos, a dynamical behavior with hypersensitivity to initial conditions, is widely studied in both classical and quantum physics [1–3]. As a prominent chaotic system, asymmetric optical microcavities have drawn much attention in diverse fields such as dynamical tunneling [4–8], optical chirality [9–12], and non-Hermitian physics [13–15]. So far, many high-performance optical devices have been promoted, including random lasers [16,17], nanoparticle sensing [18,19], and broadband optical collection [20–23]. Among these fundamental studies and practical applications, chaotic dynamics plays a pivotal role in manipulations of photon evolution in asymmetric microcavities, which is governed dominantly by manifold structures in position–momentum phase space [3,24].

Over the past decades, much effort has been devoted to exploring the manifold effects in asymmetric optical microcavities [24–33]. The manifolds have been experimentally investigated by the output from regular modes to the leaky region in an asymmetric cavity, i.e., far-field laser emission [24,33–35], or inversely, by monitoring the efficiency of free-space pumping [6,30–32]. However, all these experiments are conducted in the leaky region, while the intermediate chaotic dynamics between regular modes and the leaky region is treated as a "black box," in which the structures of manifolds are still elusive in experiments. Different from the leaky region, the intermediate region involves much richer physical processes such as scarred modes [36–38], resonance-assisted tunneling [39–41], and turnstile transport [30,33]. Hence, the illustration of manifold structures in this "black box" is important and promising for more physical research and photonic applications.

In this paper, for the first time, we open this "black box" by scanning the phase space for a high-Q optical asymmetric microcavity and observe the structure of the stable manifold. Experimentally, a nanofiber is used to continuously regulate the Birkhoff coordinates of the input light in the phase space. When the light is injected into the region with the stable manifold, the intracavity energy is confined for a long time, and its angular momentum increases rapidly. According to the

evolution of the light energy and angular momentum extracted from the transmission spectra, the stable manifold is visualized in both numerical simulations and experiments.

2. RAY-MODEL SKETCH

The asymmetric cavity is shown in Fig. 1(a), in which the real-space trajectory of light can be mapped into the phase space by the ray model [3,24,42]. Here, the phase space is spanned by Birkhoff coordinates $(\phi, \sin\chi)$ [42,43] where ϕ is the azimuthal angle and χ is the incident angle [Fig. 1(b)]. The boundary shape of the cavity used in this work is defined as $R(\phi) = R_0\Sigma_{n=2}^{6}\{1 + a_n[\cos(\phi)]^n\}$, where ϕ is the azimuthal angle, R_0 represents the radius of the cavity, and a_n is the decisive boundary parameters. Here we choose $a_2 = -0.066106$, $a_3 = -0.097356$, $a_4 = -0.0067262$, $a_5 = 0.070892$, and $a_6 = -0.0080353$ to obtain a nearly chaotic phase space. When the incident angle χ is smaller than the critical angle of total internal reflection, the light escapes into the leaky region which is bounded by the critical line $\sin\chi_c = 1/n_{\text{cavity}} \approx 0.55$ [black dashed line in Fig. 1(b)]. Note that the effective refractive index is $n_{\text{cavity}} = 1.81$ for transverse electric polarization, depending on the material ($n_{\text{silicon nitride}} = 2.02$) and geometry of the cavity (thickness = 350 nm). In the upper part of the phase space, the high-Q whispering gallery modes (WGMs) exist [44–47], supported by Kolmogorov–Arnold–Moser (KAM) curves [blue points in Fig. 1(b)] [24]. Between the KAM curves and the critical line, the region is mainly occupied by chaos, where the stable manifold forms fast channels for chaos-assisted coupling [20,30–32]. Here the stable manifold is defined as the set of points converging to the corresponding unstable periodic orbits in the forward time evolution [3,24] and behaves as a curve-like structure in the phase space [red points in Fig. 1(b)]. Note that the "stable" indicates a convergence essence of the chaotic motion. In previous work, the stable manifold is elusive in experiments due to the absence of an available approach to exciting the chaotic region [Fig. 1(c)], while in this work the stable manifold is observed by controlling the injection position in phase space [Fig. 1(d)].

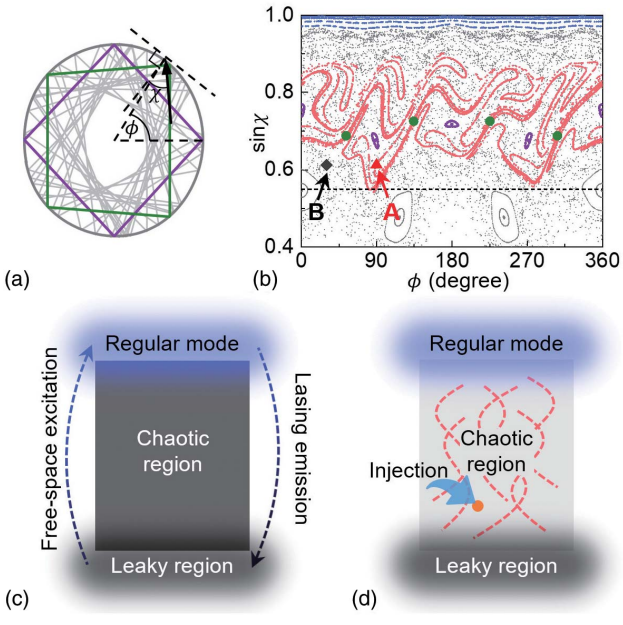

Fig. 1. (a) Chaotic ray dynamics in an asymmetric microcavity in real space. Green lines and purple lines are unstable four-period orbit and stable four-period orbit, respectively. ϕ: azimuthal angle. χ: incident angle. (b) The phase space of the chaotic microcavity. Blue points: KAM curves. Green dots: four-period unstable orbit. Purple dots: four-period stable orbit. Red points: stable manifold. Black dashed line: critical line. Point A: (90°, 0.61), near the stable manifold in the chaotic region. Point B: (30°, 0.61), in the chaotic region away from the stable manifold. (c) Investigation of the chaotic dynamics by lasing emission or free-space coupling between regular mode and leaky region, where the chaotic region is treated as a "black box." (d) Probing the stable manifold by precisely controlling the injection position in phase space.

The stable manifold that governs the chaos-assisted coupling manifests itself as the angular momentum and energy evolution of the light in the ray model. As shown in Fig. 2(a), when the Birkhoff coordinate of the input light lies near the stable manifold (point A), the angular momentum of the light, represented by $\sin\chi$, experiences a rapid increase along the stable manifold within seven reflections and holds an overall trend of increase in the following reflections. In this case, as presented in Fig. 2(c), no energy is refracted outside because the angular momentum remains above the critical line. Here the fact that the light momentum does not keep converging to the unstable period orbit [green dots in Fig. 1(b)] is due to the slight deviation from the stable manifold. This deviation comes from that we cannot choose a point exactly on the stable manifold because the manifolds are infinitesimal structures in phase space. Hence, in theory, the manifold can only be numerically obtained by initializing a bunch of points with small deviations from the unstable periodic orbit and recording their position of each

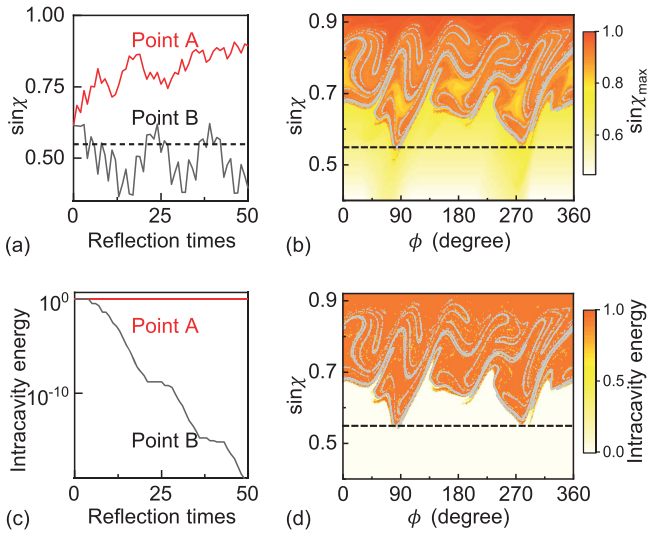

Fig. 2. (a) Angular momentum $\sin\chi$ versus reflection times starting from point A and point B as shown in Fig. 1(b). (b) Maximal angular momentum $\sin\chi_{\max}$ distribution within 50 reflections by the ray model. Gray dots: stable manifold of the four-period unstable orbit. (c) Energy intensity versus reflection times starting from point A and point B. (d) Intracavity energy distribution within 50 reflections by the ray model.

evolution, which is a widely applied strategy in studying the chaotic dynamics in deformed microcavities [3,20,24,34]. Once the initial position is away from the stable manifold (point B), the angular momentum keeps oscillating around the critical line and the energy drastically decays considering Fresnel's reflection law [26,27]. Furthermore, the maximal angular momentum and intracavity energy of each point in phase space are obtained by means of the above method as shown in Figs. 2(b) and 2(d), which is detailed as follows. (i) For the concerned phase space ($\phi \in [0°, 360°]$, $\sin\chi \in [0.4, 0.92]$), the initial points (ϕ_i, $\sin\chi_j$) are uniformly sampled (500 × 300); and (ii) the intracavity energy for each initial point (ϕ_i, $\sin\chi_j$) is obtained as $E_r(\phi_i, \sin\chi_j)$, and the maximum $\sin\chi$ for each initial point (ϕ_i, $\sin\chi_j$) is obtained as $\sin\chi_{\max}(\phi_i, \sin\chi_j)$ within 50 reflections. It is found that the maximal angular momentum and intracavity energy show a similar distribution with the stable manifold of the four-period unstable orbit. Thus, the stable manifold can be experimentally probed by initializing the position of the input light in phase space and analyzing the energy and angular momentum evolution in the chaos-assisted coupling.

3. EXPERIMENTAL CONFIGURATION

In the experiment, a silicon nitride asymmetric microdisk cavity with a thickness of 350 nm and a radius of 40 μm is placed on a rotation stage. Considering the thickness of the cavity is much less than the wavelength, a two-dimensional ray model is applicable to describe the light propagation inside the cavity. The impact from the thickness contributes to an effective refractive index, which is treated as a constant inside the cavity. Note here the boundary shape and effective refractive index of the cavity are the same as that used in the ray model. The light from a continuously tunable laser (New Focus TLB-6712) with transverse electric polarization at the 780 nm band is injected into the cavity through a tapered nanofiber with continuously variable diameters [Fig. 3(a)]. The power of input light is about 0.1 mW and thus the nonlinear effect is negligible in our experiments. To directly excite the chaotic region, the horizontal (vertical) Birkhoff coordinate of the input light ϕ_0 ($\sin\chi_0$) is controlled by the angular coupling position (effective refractive index) of the nanofiber coupler. Here the effective refractive index of the nanofiber depends on its diameter. For a specified fiber diameter and coupling azimuthal angle, the intracavity energy and angular momentum of the light can be extracted from the transmission spectra of the cavity. Note that the nanofiber is contacted to the cavity to exclude the impact by the fiber–cavity coupling gap. This nanofiber coupling technique was also applied in previous works for broadband coupling between a nanowaveguide and high-Q whispering gallery modes [20] and exploration of regular orbit engineered chaotic dynamics within a mixed phase space [48].

By scanning the wavelength of input light from 773 to 776 nm, the typical transmission spectra normalized by input power are obtained at three azimuthal angles ($\phi = 30°$, 60°, 90°) with the nanofiber diameter of 415 nm, as shown in Fig. 3(b). It is found that the spectra present two distinct features compared with that of conventional WGM coupling [49,50]: (i) the output power is mostly weaker than the input power, and (ii) the transmission spectra strongly depend on the azimuthal angles. The weak output is attributed to the fact that when the nanofiber is contacted to the cavity, the input light is mostly refracted into the cavity and may subsequently experience extra refractive loss before coupling back to the nanofiber. Hence, the intracavity energy can be characterized by the output power from the end of the nanofiber. Moreover, by experimentally initializing the input light at different positions in phase space, the light experiences distinct intracavity evolution, and the spectra exhibit strong dependences on azimuthal angles. For instance, the transmission spectrum of $\phi = 90°$ [corresponding to point A in Fig. 1(b)] is higher than that of $\phi = 30°$ [corresponding to point B in Fig. 1(b)], indicating the existence of the stable manifold therein as predicted by the ray model.

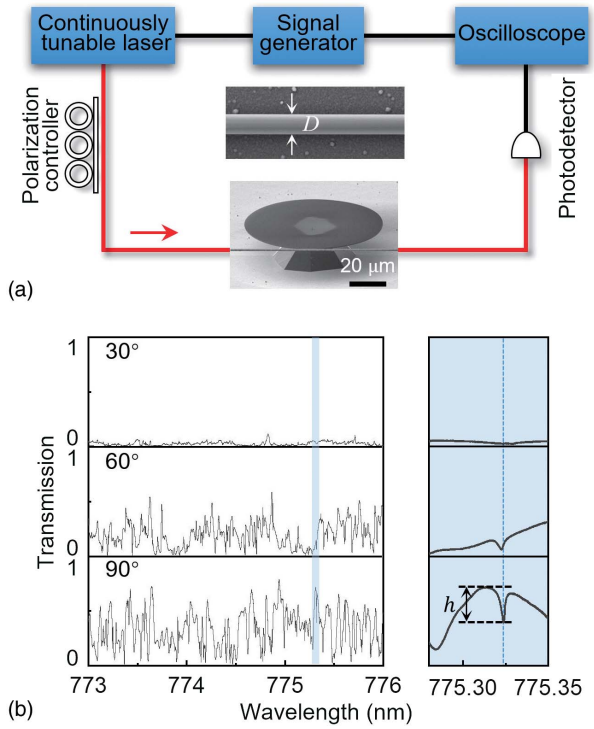

Fig. 3. (a) Schematic illustration of the fiber–cavity coupling setup. Inset: scanning electron microscope image of the fiber with a diameter of D. (b) Typical experimental transmission spectra at different azimuthal angles ($\phi = 30°$, 60°, 90°) with nanofiber diameter of 415 nm. The right panel is the zoom-in blue shadow in the spectra. The dashed line marks a same high-Q mode. The coupling depth is denoted by h.

4. RESULTS AND ANALYSES

We can visualize the stable manifold by analyzing the experimental dependence of the output power on the coupling azimuthal position ϕ, as illustrated in Figs. 4(a) and 4(b). Here, the output power is calculated as the average of the spectrum (773–776 nm), and the azimuthal angle ϕ is scanned from 30° to 150° with a step of 3° by controlling the rotation stage. The diameters of the fiber at the coupling position are chosen as 415 and 530 nm, corresponding to the two lines that cross the region with a clear structure of the stable manifold in phase space [Fig. 4(c)].

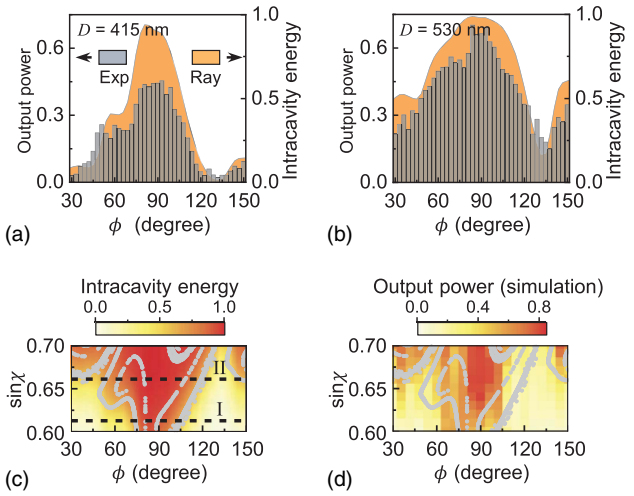

Fig. 4. (a), (b) Experimental output power (gray histograms) versus the excitation azimuthal angles in experiments with nanofiber diameters of 415 nm and 530 nm, respectively. The waterfall plots present corresponding intracavity energy by the ray model. (c) Intracavity energy distribution by the modified ray model. Gray points: stable manifold. The black dashed line I (II) marks the corresponding experimental position, i.e., fiber diameters of 415 nm (530 nm), in phase space. (d) Distribution of the output power obtained by 2D-FDTD simulations, covering the same region as (c).

Note here we employ a modified ray model to obtain Fig. 4(c) from Fig. 2(d) considering the wave diffusion. In the wave optics regime, the initial state of the input light is not a single point but approximately a 2D Gaussian distribution, and thus the intracavity energy and maximum $\sin\chi$ need to be modified. The formula of Gaussian distribution versus a given initial point $(\phi_0, \sin\chi_0)$ is presented as follows:

$$G(\phi_i, \sin\chi_j)|_{\phi_0, \sin\chi_0} = \frac{1}{2\pi\sigma_1\sigma_2} e^{-\frac{(\phi_i-\phi_0)^2}{\sigma_1^2} - \frac{(\sin\chi_j-\sin\chi_0)^2}{\sigma_2^2}}, \quad (1)$$

where $\sigma_1 = 0.034$ and $\sigma_2 = 2.86°$ obtained by the simulation of a cavity with experimental size ($R_0 = 40$ μm). The modified distribution of the intracavity energy $E_r'(\phi_0, \sin\chi_0)$ is calculated as follows:

$$E_r'(\phi_0, \sin\chi_0) = \sum_{i=1}^{500}\sum_{j=1}^{300} \mathrm{E}_r(\phi_i, \sin\chi_j) G(\phi_i, \sin\chi_j)|_{\phi_0, \sin\chi_0}. \quad (2)$$

Compared with the modified intracavity energy [waterfall plots in Figs. 4(a) and 4(b)] by the ray model, the experimental output power behaves as a similar distribution and thus can be used for the probe of the stable manifold. When the diameter is 415 nm, the output power in measurements [gray histograms in Fig. 4(a)] manifests one main peak around $\phi = 90°$, where the stable manifold lies. In contrast, the output power is much weaker in the region away from the stable manifold. When it comes to the fiber diameter of 530 nm, the output power [gray histograms in Fig. 4(b)] becomes stronger on the whole, due to the increasing overlap between line II and the stable manifold. Notice that the experimental output still presents a peak around 90° despite the absence of the stable manifold. This counterintuitive phenomenon arises from the fact that a four-period island structure exists around (90°, 0.61), resulting in energy localization and low refractive loss [7,34,48,51].

Numerically, we conduct the two-dimensional finite-difference time-domain (2D-FDTD) simulations, covering the region with $\phi \in [30°, 150°]$ and $\sin\chi \in [0.6, 0.7]$. The parameters in the simulation are set the same as those used in experiments ($R = 40$ μm), but in a two-dimensional model due to the limitation of computing resources. By controlling the coupling azimuthal angle (coupler size), the coordinate ϕ ($\sin\chi$) is scanned with a step of 6° (0.01). The averaged output power under different input conditions is plotted in Fig. 4(d), exhibiting the consistent pattern compared with the stable manifold as well as the intracavity energy distribution by the ray model [Fig. 4(c)].

Besides the energy evolution, the stable manifold is also visualized by angular momentum transformation, which can be characterized by the transmission spectra of high-Q regular modes. As shown in Fig. 1(d), the high-Q regular modes are established by the following three steps: (i) injection of the light into the cavity; (ii) the angular momentum transformation of the light in the chaotic region [Fig. 2(a)] [20]; and (iii) dynamical tunneling into the KAM curves and forming high-Q WGMs [6,8]. When the injection lies near the stable manifold, the angular momentum of the light can experience a rapid increase, resulting in the stronger coupling to high-Q modes, which is confirmed by comparing the coupling depth h at $\phi = 90°$ and $\phi = 30°$ in Fig. 3(b).

Experimentally, eight modes with $Q > 10^5$ are selected on the transmission spectra, and the averaged coupling depths versus azimuthal angles are plotted in Figs. 5(a) and 5(b), corresponding to line I and line II in Fig. 5(c), respectively. Note here we employ a modified ray model to obtain Fig. 5(c) from

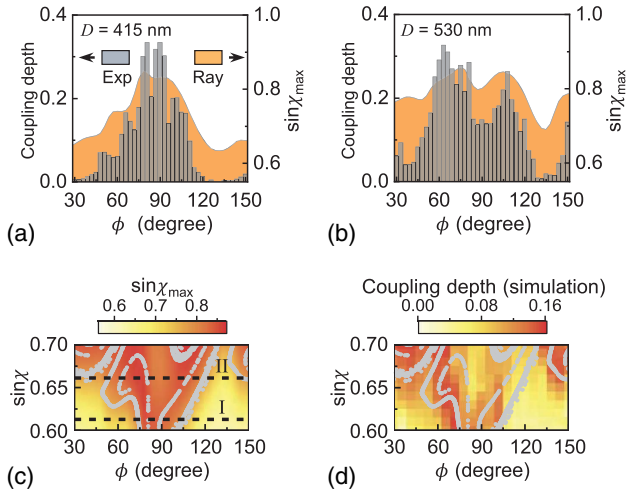

Fig. 5. (a), (b) Experimental coupling depth of high-Q modes (gray histograms) versus the excitation azimuthal angles in experiments with nanofiber diameters of 415 and 530 nm and corresponding $\sin\chi_{max}$ (waterfall plots) obtained in the ray model. (c) Modified $\sin\chi_{max}$ distribution magnified from Fig. 2(b). (d) Distribution of the coupling depth of high-Q modes extracted from 2D-FDTD simulations, covering the same region as (c).

Fig. 2(b) considering the wave diffusion. The momentum transformation $\sin\chi'_{\max}(\phi_0, \sin\chi_0)$ is calculated as follows:

$$\sin\chi'_{\max}(\phi_0, \sin\chi_0) = \sum_{i=1}^{500}\sum_{j=1}^{300} \sin\chi_{\max}(\phi_i, \sin\chi_j)G(\phi_i, \sin\chi_j)|_{\phi_0, \sin\chi_0}. \quad (3)$$

For the diameter of the fiber being 415 nm, it is found that the stronger coupling occurs around $\phi = 90°$, manifesting the existence of the stable manifold, which also agrees with the results of energy evolution. When the fiber diameter is chosen as 530 nm, four peaks arise around 33°, 63°, 108°, and 150°, depicting the distribution of the stable manifold along line II in Fig. 5(c). Note that here a valley appears around 90°, which is attributed to the localization effect of the island structure. Additionally, the $\sin\chi_{\max}$ is also plotted in Figs. 5(a) and 5(b), presenting the same behavior as the experimental coupling depths of high-Q modes. By performing the 2D-FDTD simulation, the coupling depth of high-Q modes from spectra is also investigated, shown in Fig. 5(d). The simulation setting is the same as that in Fig. 4(d), and eight cavity modes with $Q > 7 \times 10^4$ are selected, which are confirmed as WGM-like regular modes by the simulated field distributions. It is found that the coupling depth distribution by simulations [Fig. 5(d)] exhibits good agreement with the $\sin\chi_{\max}$ distribution by the ray model [Fig. 5(c)]. Consequently, by applying this numerical dense sampling, the quasi-continuous distribution of the stable manifold within the region $\phi \in [30°, 150°]$ and $\sin\chi \in [0.6, 0.7]$ is traced out by the high contrast of the coupling depth.

5. CONCLUSION

Up to now, we have demonstrated the observation of the stable manifold in simulations and experiments. On the one hand, the stable manifold can be clearly depicted in the ray model [see Figs. 2(b) and 2(d)], but wave effects are excluded. On the other hand, the fine structure in phase space is blurred in the wave region, leading to a limited observation resolution both in experiments and simulations [see Figs. 4 and 5]. Meanwhile, the modified ray model employed here combines the ray model and the wave diffusion effect, which presents good agreement with the experimental and simulated results. Considering that the diffused size of input light in phase space negatively relies on the ratio of cavity diameter to wavelength, the resolution for the observation of the stable manifold can be enhanced by decreasing the light wavelength or increasing the cavity size.

To summarize, we demonstrate the observation of the stable manifold in the phase space of an asymmetric microcavity characterized by energy evolution and momentum transformation of the intracavity light. Experimentally, the structure of the stable manifold is depicted by the output power and the coupling depth to high-Q modes, which is further confirmed by the numerical simulations and ray-model prediction. In addition, we point out that the strategy proposed in our work can be further optimized by taking more detailed effects into consideration, such as the dynamical tunneling process and the impact of the unstable manifold. This characterization of the manifold structures not only experimentally demonstrates the manifold theory but also provides a guidance for regulation of the chaotic dynamics as well as the associated optical properties. This developed experimental method provides a versatile method to study chaotic dynamics and holds great potential for the reconstruction of complex structures in the phase space of a chaotic system. Beyond the fundamental study, the exploration of the chaotic dynamics also provides an approach to control the photon by different initialization of the input light in asymmetric optical microcavities. Considering the abundant physical phenomena happening in the chaotic region, this work can also contribute to advanced photonic applications, such as broadband optical communications [23, 52] and on-chip chaotic neural networks [53].

Funding. National Key Research and Development Program of China (2016YFA0301302, 2018YFB2200401); National Natural Science Foundation of China (11825402, 11654003, 61435001, 11527901, 12041602); Key Research and Development Program of Guangdong Province (2018B030329001); National Postdoctoral Program for Innovative Talents (BX20200014); China Postdoctoral Science Foundation (2020M680185).

Acknowledgment. The authors thank Y.-Q. Nie, X.-C. Yu, Y.-Y. Li, H.-J. Chen, J.-H. Chen, D. Xu, S.-J. Tang, P.-J. Zhang, and L. Yao for helpful discussions. This work was partially carried out at the USTC Center for Micro and Nanoscale Research and Fabrication, and the High-Performance Computing Platform of Peking University.

Disclosures. The authors declare no conflicts of interest.

†These authors contributed equally to this paper.

REFERENCES

1. R. C. Hilborn, *Chaos and Nonlinear Dynamics: An Introduction for Scientists and Engineers* (Oxford University Press, 2000).
2. M. C. Gutzwiller, *Chaos in Classical and Quantum Mechanics* (Springer, 2013).
3. H. Cao and J. Wiersig, "Dielectric microcavities: model systems for wave chaos and non-Hermitian physics," Rev. Mod. Phys. **87**, 61–111 (2015).
4. V. A. Podolskiy and E. E. Narimanov, "Chaos-assisted tunneling in dielectric microcavities," Opt. Lett. **30**, 474–476 (2005).
5. A. Bäcker, R. Ketzmerick, S. Löck, J. Wiersig, and M. Hentschel, "Quality factors and dynamical tunneling in annular microcavities," Phys. Rev. A **79**, 063804 (2009).
6. J. Yang, S.-B. Lee, S. Moon, S.-Y. Lee, S. W. Kim, T. T. A. Dao, J.-H. Lee, and K. An, "Pump-induced dynamical tunneling in a deformed microcavity laser," Phys. Rev. Lett. **104**, 243601 (2010).
7. Q. Song, L. Ge, B. Redding, and H. Cao, "Channeling chaotic rays into waveguides for efficient collection of microcavity emission," Phys. Rev. Lett. **108**, 243902 (2012).
8. Q.-F. Yang, X.-F. Jiang, Y.-L. Cui, L. Shao, and Y.-F. Xiao, "Dynamical tunneling-assisted coupling of high-Q deformed microcavities using a free-space beam," Phys. Rev. A **88**, 023810 (2013).
9. G. Chern, H. Tureci, A. D. Stone, R. Chang, M. Kneissl, and N. Johnson, "Unidirectional lasing from InGaN multiple-quantum-well spiral-shaped micropillars," Appl. Phys. Lett. **83**, 1710–1712 (2003).

10. B. Redding, L. Ge, Q. Song, J. Wiersig, G. S. Solomon, and H. Cao, "Local chirality of optical resonances in ultrasmall resonators," Phys. Rev. Lett. **108**, 253902 (2012).
11. R. Sarma, L. Ge, J. Wiersig, and H. Cao, "Rotating optical microcavities with broken chiral symmetry," Phys. Rev. Lett. **114**, 053903 (2015).
12. S. Liu, J. Wiersig, W. Sun, Y. Fan, L. Ge, J. Yang, S. Xiao, Q. Song, and H. Cao, "Transporting the optical chirality through the dynamical barriers in optical microcavities," Laser Photonics Rev. **12**, 1800027 (2018).
13. S.-B. Lee, J. Yang, S. Moon, S.-Y. Lee, J.-B. Shim, S. W. Kim, J.-H. Lee, and K. An, "Observation of an exceptional point in a chaotic optical microcavity," Phys. Rev. Lett. **103**, 134101 (2009).
14. C.-H. Yi, J. Kullig, and J. Wiersig, "Pair of exceptional points in a microdisk cavity under an extremely weak deformation," Phys. Rev. Lett. **120**, 093902 (2018).
15. C.-H. Yi, J. Kullig, M. Hentschel, and J. Wiersig, "Non-Hermitian degeneracies of internal–external mode pairs in dielectric microdisks," Photon. Res. **7**, 464–472 (2019).
16. S. Bittner, S. Guazzotti, X. Hu, H. Yilmaz, K. Kim, Y. Zeng, S. S. Oh, Q. J. Wang, O. Hess, and H. Cao, "Suppressing spatio-temporal lasing instabilities with wave-chaotic microcavities," Science **361**, 1225–1231 (2018).
17. S. Bittner, K. Kim, Y. Zeng, Q. J. Wang, and H. Cao, "Spatial structure of lasing modes in wave-chaotic semiconductor microcavities,"New J. Phys., **22**, 083002 (2020).
18. L. Shao, X.-F. Jiang, X.-C. Yu, B.-B. Li, W. R. Clements, F. Vollmer, W. Wang, Y.-F. Xiao, and Q. Gong, "Detection of single nanoparticles and lentiviruses using microcavity resonance broadening," Adv. Mater. **25**, 5616–5620 (2013).
19. N. Zhang, Z. Gu, S. Liu, Y. Wang, S. Wang, Z. Duan, W. Sun, Y.-F. Xiao, S. Xiao, and Q. Song, "Far-field single nanoparticle detection and sizing," Optica **4**, 1151–1156 (2017).
20. X. Jiang, L. Shao, S. X. Zhang, X. Yi, J. Wiersig, L. Wang, Q. Gong, M. Lončar, L. Yang, and Y. F. Xiao, "Chaos-assisted broadband momentum transformation in optical microresonators," Science **358**, 344–347 (2017).
21. L. Ge, "Quantum chaos in optical microcavities: a broadband application," Europhys. Lett. **123**, 64001 (2018).
22. L. Wang, C. Wang, J. Wang, F. Bo, M. Zhang, Q. Gong, M. Lončar, and Y.-F. Xiao, "High-*Q* chaotic lithium niobate microdisk cavity," Opt. Lett. **43**, 2917–2920 (2018).
23. H.-J. Chen, Q.-X. Ji, H. Wang, Q.-F. Yang, Q.-T. Cao, Q. Gong, X. Yi, and Y.-F. Xiao, "Chaos-assisted two-octave-spanning microcombs," Nat. Commun. **11**, 2336 (2020).
24. H. G. Schwefel, N. B. Rex, H. E. Tureci, R. K. Chang, A. D. Stone, T. Ben-Messaoud, and J. Zyss, "Dramatic shape sensitivity of directional emission patterns from similarly deformed cylindrical polymer lasers," J. Opt. Soc. Am. B **21**, 923–934 (2004).
25. S.-Y. Lee, S. Rim, J.-W. Ryu, T.-Y. Kwon, M. Choi, and C.-M. Kim, "Quasiscarred resonances in a spiral-shaped microcavity," Phys. Rev. Lett. **93**, 164102 (2004).
26. J. Ryu, S. Y. Lee, C. Kim, and Y. Park, "Survival probability time distribution in dielectric cavities," Phys. Rev. E **73**, 036207 (2006).
27. J. Wiersig and M. Hentschel, "Combining directional light output and ultralow loss in deformed microdisks," Phys. Rev. Lett. **100**, 033901 (2008).
28. S. Shinohara, T. Fukushima, and T. Harayama, "Light emission patterns from stadium-shaped semiconductor microcavity lasers," Phys. Rev. A **77**, 033807 (2008).
29. E. G. Altmann, "Emission from dielectric cavities in terms of invariant sets of the chaotic ray dynamics," Phys. Rev. A **79**, 013830 (2009).
30. J. Yang, S.-B. Lee, J.-B. Shim, S. Moon, S.-Y. Lee, S. W. Kim, J.-H. Lee, and K. An, "Enhanced nonresonant optical pumping based on turnstile transport in a chaotic microcavity laser," Appl. Phys. Lett. **93**, 061101 (2008).
31. J. Yang, S. Lee, S. Moon, S. Y. Lee, S. W. Kim, and K. An, "Observation of resonance effects in the pump transmission of a chaotic microcavity," Opt. Express **18**, 26141–26148 (2010).
32. F. Shu, C. Zou, and F. Sun, "Dynamic process of free space excitation of asymmetric resonant microcavity," J. Lightwave Technol. **31**, 1884–1889 (2013).
33. J.-B. Shim, S.-B. Lee, S. W. Kim, S.-Y. Lee, J. Yang, S. Moon, J.-H. Lee, and K. An, "Uncertainty-limited turnstile transport in deformed microcavities," Phys. Rev. Lett. **100**, 174102 (2008).
34. S. Shinohara, T. Harayama, T. Fukushima, M. Hentschel, T. Sasaki, and E. E. Narimanov, "Chaos-assisted directional light emission from microcavity lasers," Phys. Rev. Lett. **104**, 163902 (2010).
35. S. Shinohara, T. Harayama, T. Fukushima, M. Hentschel, S. Sunada, and E. E. Narimanov, "Chaos-assisted emission from asymmetric resonant cavity microlasers," Phys. Rev. A **83**, 053837 (2011).
36. E. J. Heller, "Bound-state eigenfunctions of classically chaotic Hamiltonian systems: scars of periodic orbits," Phys. Rev. Lett. **53**, 1515–1518 (1984).
37. S. B. Lee, J. H. Lee, J. S. Chang, H. J. Moon, S. W. Kim, and K. An, "Observation of scarred modes in asymmetrically deformed microcylinder lasers," Phys. Rev. Lett. **88**, 033903 (2002).
38. N. Rex, H. E. Tureci, H. Schwefel, R. Chang, and A. D. Stone, "Fresnel filtering in lasing emission from scarred modes of wave-chaotic optical resonators," Phys. Rev. Lett. **88**, 094102 (2002).
39. H. Kwak, Y. Shin, S. Moon, S.-B. Lee, J. Yang, and K. An, "Nonlinear resonance-assisted tunneling induced by microcavity deformation," Sci. Rep. **5**, 9010 (2015).
40. S. Gehler, S. Löck, S. Shinohara, A. Bäcker, R. Ketzmerick, U. Kuhl, and H.-J. Stöckmann, "Experimental observation of resonance-assisted tunneling," Phys. Rev. Lett. **115**, 104101 (2015).
41. F. Fritzsch, R. Ketzmerick, and A. Bäcker, "Resonance-assisted tunneling in deformed optical microdisks with a mixed phase space," Phys. Rev. E **100**, 042219 (2019).
42. J. Nöckel, A. Stone, and R. Chang, "*Q* spoiling and directionality in deformed ring cavities," Opt. Lett. **19**, 1693–1695 (1994).
43. G. D. Birkhoff, "On the periodic motions of dynamical systems," Acta Math. **50**, 359–379 (1927).
44. K. J. Vahala, "Optical microcavities," Nature **424**, 839–846 (2003).
45. Q. Song, "Emerging opportunities for ultra-high *Q* whispering gallery mode microcavities," Sci. China Phys. Mech. Astron. **62**, 074231 (2019).
46. J. Ward and O. Benson, "WGM microresonators: sensing, lasing and fundamental optics with microspheres," Laser Photonics Rev. **5**, 553–570 (2011).
47. Y.-D. Yang, M. Tang, F.-L. Wang, Z.-X. Xiao, J.-L. Xiao, and Y.-Z. Huang, "Whispering-gallery mode hexagonal micro-/nanocavity lasers," Photon. Res. **7**, 594–607 (2019).
48. L.-K. Chen, Y.-Z. Gu, Q.-T. Cao, Q. Gong, J. Wiersig, and Y.-F. Xiao, "Regular-orbit-engineered chaotic photon transport in mixed phase space," Phys. Rev. Lett. **123**, 173903 (2019).
49. M. Cai, O. Painter, and K. J. Vahala, "Observation of critical coupling in a fiber taper to a silica-microsphere whispering-gallery mode system," Phys. Rev. Lett. **85**, 74–77 (2000).
50. D. Armani, T. Kippenberg, S. Spillane, and K. Vahala, "Ultra-high-Q toroid microcavity on a chip," Nature **421**, 925–928 (2003).
51. H. E. Tureci, H. G. L. Schwefel, A. D. Stone, and E. E. Narimanov, "Gaussian-optical approach to stable periodic orbit resonances of partially chaotic dielectric micro-cavities," Opt. Express **10**, 752–776 (2002).
52. J. Wang, Z. Lu, W. Wang, F. Zhang, J. Chen, Y. Wang, J. Zheng, S. T. Chu, W. Zhao, X. Q. Little, E. Brent, and W. Zhang, "Long-distance ranging with high precision using a soliton microcomb," Photon. Res. **8**, 1964–1972 (2020).
53. S. Sunada and A. Uchida, "Photonic reservoir computing based on nonlinear wave dynamics at microscale," Sci. Rep. **9**, 19078 (2019).